ACS APPLIED MATERIALS & INTERFACES
Research Article
www.acsami.org

Walnut-like Porous Core/Shell TiO_2 with Hybridized Phases Enabling Fast and Stable Lithium Storage

Yi Cai,[†] Hong-En Wang,*[,†,‡] Xu Zhao,[‡] Fei Huang,[‡] Chao Wang,[†] Zhao Deng,[†] Yu Li,[†] Guozhong Cao,*[,‡] and Bao-Lian Su*[,†,§,∥]

[†]State Key Laboratory of Advanced Technology for Materials Synthesis and Processing, Wuhan University of Technology, 122 Luoshi Road, 430070, Wuhan, Hubei, China

[‡]Department of Materials Science and Engineering, University of Washington, Seattle, Washington 98195-2120, United States

[§]Laboratory of Inorganic Materials Chemistry (CMI), University of Namur, 61 rue de Bruxelles, B-5000 Namur, Belgium

[∥]Department of Chemistry and Clare Hall, University of Cambridge, Cambridge CB2 1EW, U.K.

Supporting Information

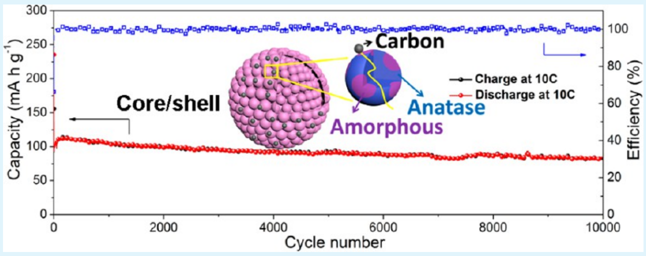

ABSTRACT: TiO_2 is a promising and safe anode material for lithium ion batteries (LIBs). However, its practical application has been plagued by its poor rate capability and cycling properties. Herein, we successfully demonstrate a novel structured TiO_2 anode with excellent rate capability and ultralong cycle life. The TiO_2 material reported here shows a walnut-like porous core/shell structure with hybridized anatase/amorphous phases. The effective synergy of the unique walnut-like porous core/shell structure, the phase hybridization with nanoscale coherent heterointerfaces, and the presence of minor carbon species endows the TiO_2 material with superior lithium storage properties in terms of high capacity (~177 mA h g^{-1} at 1 C, 1 C = 170 mA g^{-1}), good rate capability (62 mA h g^{-1} at 100 C), and excellent cycling stability (~83 mA h g^{-1} was retained over 10 000 cycles at 10 C with a capacity decay of 0.002% per cycle).

KEYWORDS: *anatase, amorphous, TiO_2, titanate, porous core/shell structure, lithium ion battery, anode material, electrochemical performance*

1. INTRODUCTION

Lithium ion batteries (LIBs) are a very promising electrochemical power source that are widely used in portable electronics, electric vehicles, and stationary energy storage systems because of their environmental friendliness, long calendar life, high output voltage, and energy density.[1] Currently, graphite is the main anode material for commercial LIBs; however, it still suffers from poor rate capability and low safety.[2] Several alternative candidates, such as alloy-based materials[3,4] and transition metal oxides and sulfides,[5−7] have been explored as next-generation anode materials for LIBs. Among them, titanium dioxide (TiO_2) has attracted much attention because of its low cost, environmental benignity, and structural stability. Moreover, TiO_2 is electrochemically stable during lithaition/delithiation processes, and it can avoid lithium electroplating which causes safety concerns. However, the practical application of TiO_2 in LIBs has been hindered by the large polarization at high charge/discharge rates due to the sluggish Li^+ diffusion and poor electron transport. To mitigate the slow kinetics, many approaches have been studied, such as engineering the particle morphology and size, phase composition, oxygen vacancies, and surface modification to improve the battery performance by enhancing the ionic diffusion and electronic conduction.[8−11]

Previous studies have demonstrated that reducing the particle sizes of TiO_2 to nanoscale range could significantly improve the Li^+ insertion/extraction kinetics and increase the storage capacity.[12,13] To this end, various low-dimensional nanostructured TiO_2, such as nanoparticles,[14] nanorods/nanowires,[15,16] nanotubes,[17,18] nanocables,[19] and nanosheets,[20] have been synthesized to improve the performance. For example, an alkaline hydrothermal process has been developed to synthesize various 1D TiO_2 nanostructures anodes using amorphous or crystalline TiO_2 nanoparticles as starting precursors.[15,16] Further, to overcome the easy aggregation of low-dimensional nanostructures, porous and hollow TiO_2 nanostructures having unique structural superiorities of both nanosized building units and microsized assemblies are thus able to manifest enhanced strain-accommodation capability and structural stability.[21,22] In particular, porous core/shell TiO_2 materials are more appealing because of their high surface area and permeability to electrolyte as well as the ability to better accommodate the repeated volume variation upon electrochemical cycling.[23−26] Meanwhile, introducing conductive

Received: December 23, 2016
Accepted: March 7, 2017
Published: March 7, 2017

DOI: 10.1021/acsami.6b16498
ACS Appl. Mater. Interfaces 2017, 9, 10652−10663

Scheme 1. Schematic Illustration of the Formation Process of the Porous Core/Shell TiO_2: (a) Amorphous TiO_2/Oleylamine Precursor, (b) Porous Sodium Titanate (NaTiO), (c) Porous Core/Shell Hydrogen Titanate (HTiO), and (d) Porous Core/Shell TiO_2

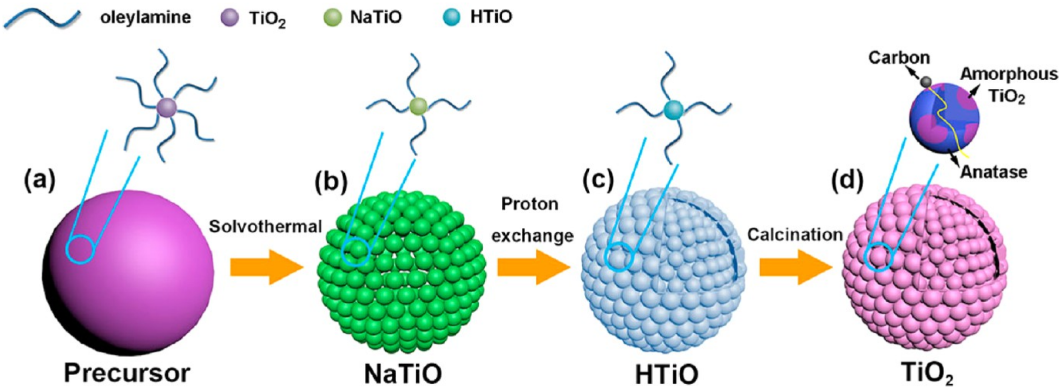

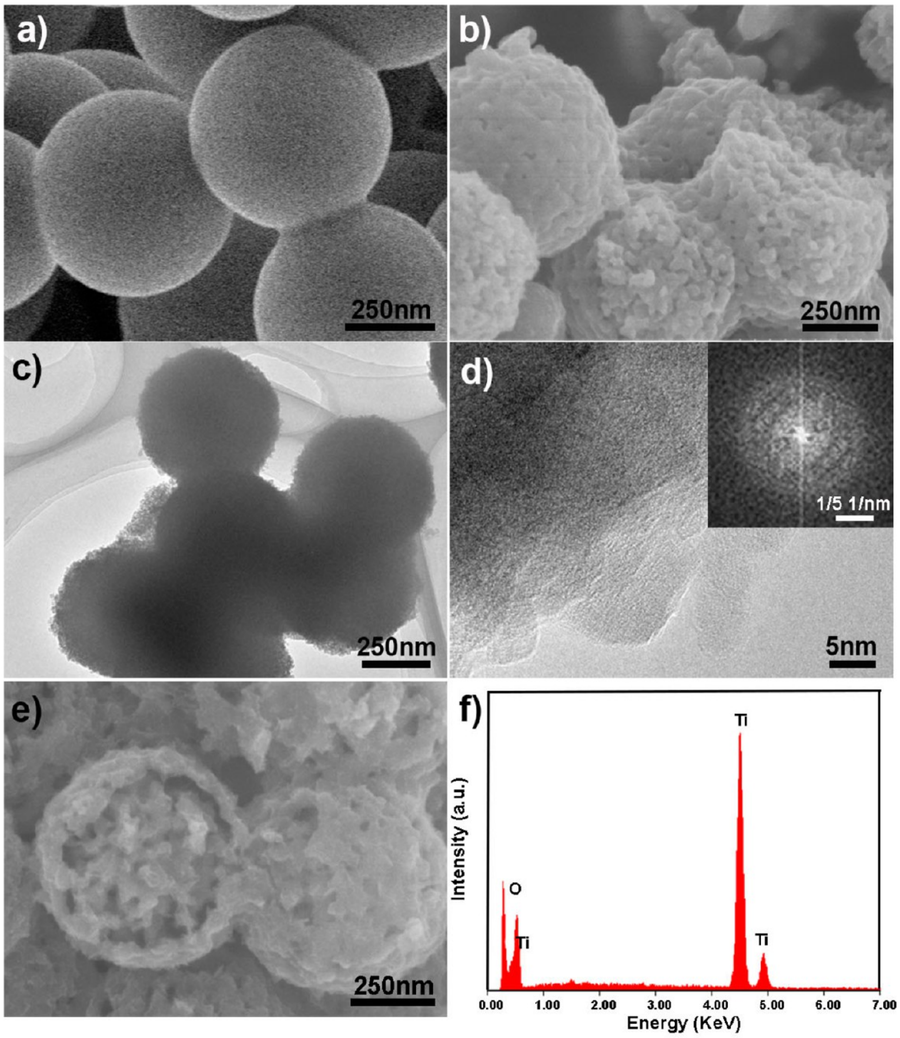

Figure 1. SEM images of the (a) amorphous TiO_2/oleylamine precursor, (b) sodium titanate (NaTiO); (c, d) TEM images and FFT pattern (inset of d) of NaTiO (the diffused circle in the FFT pattern reveals the amorphous characteristic of the NaTiO product); (e) SEM image and (f) EDX pattern of the hydrogen titanate (HTiO) product, demonstrating apparently the complete replacement of Na^+ with H^+.

materials is also an effective approach to improve the lithium storage performance of TiO_2 because it can significantly enhance the electron transport of the electrode.[27] Furthermore, previous studies have suggested that the formed Ti−C bond between TiO_2 and conductive carbon materials can strongly boost the electrical conductivity which is different from the weak physical contact.[28−30] For example, Etacheri et al.[30] synthesized chemically bonded TiO_2−B nanosheet/reduced graphene oxide hybrid via a simple photocatalytic reduction method. Benefiting from the synergistic effects of the increased charge transfer with Ti−C bond and exposed (010) facets, the nanocomposite presents good rate performance and excellent cycling stability.

In addition, engineering the TiO_2 materials with mixed polymorphs has also been proposed to improve the lithium storage performance. Through coupling the anatase TiO_2 with secondary TiO_2−B or amorphous TiO_2, the lithium storage capability could been significantly improved,[31−34] because the multiphased TiO_2 hybrid shows unique phase boundaries, which can improve the Li-ion diffusion and facilitate electron transport through the electrode.[31,33] For example, Guo et al.[31] designed and fabricated surface amorphized TiO_2@graphene hybrids for LIBs. The surface amorphized sample exhibited improved lithium storage performance compared with crystalline sample owing to the lower lithium-ion diffusion and electronic conduction resistances and better surface adsorption in the amorphous layer.

Herein, inspired by all the above considerations, we have successfully fabricated a porous walnut-like TiO_2/C core/shell structure with hybridized anatase/amorphous phases and incorporation of minor carbon species in form of Ti−C chemical bond. The material was prepared by an alkaline solvothermal process paired with post-treatment using well-defined TiO_2/oleylamine hybrid spheres as precursor. Our finding is strikingly different from the most conventional alkaline hydrothermal processes whereas phase-pure one-dimensional TiO_2 nanostructures or their assemblies are routinely obtained. Interestingly, the synergy of porous core/shell nanostructures, hybridized anatase/amorphous phases with nanoscale coherent interfaces, and favorable Ti−C bonds endows the TiO_2 hybrid material with superfast Li^+ diffusion and electron transport and enhanced pseudocapacitive lithium storage, giving rise to excellent lithium storage capability. Through the *ex situ* characterizations, we also observe the existence of cubic $LiTiO_2$ nanodots attaching on the electrode surface after long-term discharge/recharge processes, which strongly supports the deep lithiation capability of the porous core/shell TiO_2 electrode.

2. RESULTS AND DISCUSSION

The porous core/shell TiO_2 material was synthesized by an alkaline solvothermal reaction paired with post-treatment, as illustrated in Scheme 1. First, amorphous TiO_2/oleylamine precursor (Scheme 1a) was fabricated by sol−gel processing and used as a self-template in the subsequent process. The resulting TiO_2/oleylamine precursor consists of uniformly sized spherical particles with smooth surface and diameter of ∼500 nm as revealed by means of scanning electron microscopy (SEM) (Figure 1a).

The precursor was *in situ* converted into sodium titanates (termed as NaTiO, Scheme 1b) by a solvothermal reaction in alkaline solution. It is noted that the resulting NaTiO product consists of porous spheres made of nanoparticles (Figures 1b−d). The X-ray diffraction (XRD) pattern further reveals its amorphous nature or very poor crystallinity (Figure 2a). This finding is noticeably different from the crystalline titanate nanowires/nanotubes/nanofibers commonly reported in the literature.[15,16] To probe the formation process of the porous amorphous NaTiO spheres, a series of intermediate products at different stages of solvothermal synthesis were collected and analyzed by SEM (Figure S1). It is clear that porous NaTiO spheres were formed within a short reaction period of 3 h (Figure S1a). Further prolonged reaction time up to 12 h did not change much of the porous spherical morphologies but only enlarged the pores in the spheres (Figure S1b−d). On the basis of these observations, we hypothesize that the high alkaline concentration and presence of oleylamine species in the TiO_2 precursor play an important role in controlling the formation of such porous amorphous NaTiO spheres. On the one hand, at high alkali concentration the NaOH can penetrate into the loose hybrid spheres and react with TiO_2 colloids, favoring rapid formation of a large number of titanate nuclei shortly. On the other hand, the chemisorption of oleylamine molecules on the surfaces of the titanate nuclei would hinder their further attachment and crystallization into low-dimensional nanostructures.

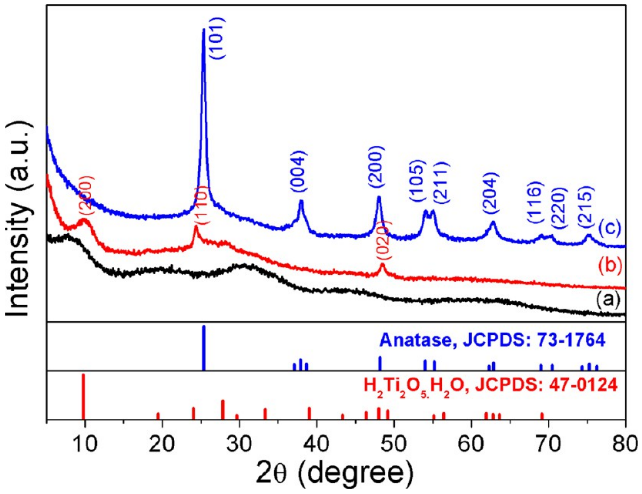

Figure 2. XRD patterns of the as-prepared (a) sodium titanate (NaTiO), (b) hydrogen titanate (HTiO), and (c) TiO_2 product.

After the proton-exchange process, the resulting hydrogen titanate (HTiO) sample (Scheme 1c) consists of core/shell spherical structures (Figure 1e), differing from its parent NaTiO product. The HTiO shell of ∼30 nm thickness is mainly composed of interconnected nanoparticles. The inner porous core with a diameter of ∼400 nm is also composed of interlinked nanoparticles. The XRD pattern (Figure 2b) reveals the HTiO sample is crystallized, and the diffraction reflections can be readily indexed to orthorhombic $H_2Ti_2O_5{\cdot}H_2O$ phase (JCPDS Card No. 47-0124).[35] The formation of such unique core−shell structure can be explained by the Kirkendall effect, which deals with the movement of the interface between two diffusion couples during the ion-exchange process.[36] In current experiments, the protons (H^+) in the acid solution acting as diffusion species would exchange with Na^+ ions in the NaTiO. The diffusion at (NaTiO) solid/solution interface and the concentration gradients of H^+ and Na^+ within each phase would lead to the original formation of a $H_2Ti_2O_5{\cdot}H_2O$ shell. In addition, the exchange of Na^+ with protons is thermodynamically favorable. The energy gain during the proton-exchange process can promote the crystallization of the HTiO shell. As a result, the rigid and crystalline HTiO shell would then detach from the inner core, leading to the formation of a core/shell HTiO structure. In addition, no Na element is detected in the energy-dispersive X-ray (EDX) pattern (Figure 1f), which apparently verifies the complete replacement of Na^+ by H^+ after ion exchange.

Finally, porous core/shell TiO_2 was obtained after dehydration of the HTiO by heat treatment at 300 °C in air (Scheme 1d). The XRD reflections (Figure 2c) can be readily indexed to the tetragonal anatase phase (JCPDS Card No. 21-1272).[37,38] The broadening of the diffraction reflections suggests the relatively low crystallinity due to possible existence of amorphous TiO_2 components in the as-obtained product because of the low calcination temperature used. Raman spectroscopy (Figure 3) was further performed to demonstrate the crystal structure of TiO_2, where five apparent Raman peaks at 150, 198, 395, 515, and 634 cm^{-1} can be observed, corresponding to the typical Raman modes of anatase TiO_2.[39] From the SEM image in Figure 4a, the spherical structure has been well preserved and many macropores (∼55 nm) can be observed on the particle surface. SEM image of several broken spheres (Figure 4b) further unravels the porous core/shell structure of the resulting TiO_2 material. TEM image confirms the shell has a thickness of ∼30 nm and is constructed by some nanoparticles and nanosheets (Figure 4c). The inner porous core is composed of some aggregated nanoparticles with interconnected pore channels. The highly porous core/shell structure can afford a large contact area for the wettability of electrode with electrolyte and a short diffusion pathway for Li^+ and electron transport. Clear lattice fringes with a spacing of 0.35 nm in the HRTEM micrograph can be assigned to the (101) and (011) crystal planes of anatase (Figure 4d). In addition, some amorphous TiO_2 domains can also be observed as labeled by the dotted and closed yellow lines. The amorphous domains surround the anatase nanocrystals, forming abundant continuous coherent heterointerfaces on a nanoscale (Figure S2). The formation of amorphous domains can be attributed to the low annealing temperature and the existence of minor oleylamine molecules in the HTiO product, which decompose into carbon species during annealing and suppress the crystallization of TiO_2. The existence of amorphous domains can potentially increase the lithium storage capability of the TiO_2 material. (1) Amorphous TiO_2 has a higher practical lithium storage capacity and can better buffer the volume change during charge/discharge due to its loose structure and low mass density.[40] (2) The heterojunctions created at the anatase/amorphous interface can enhance the

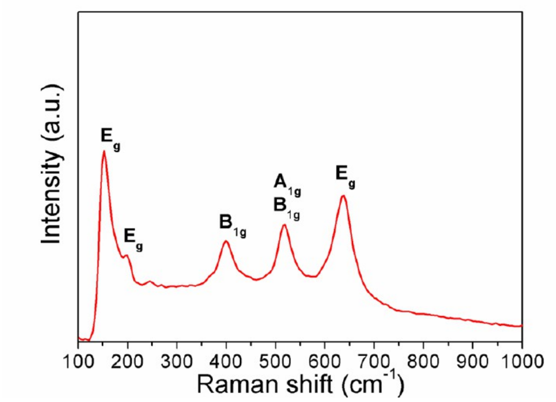

Figure 3. Raman spectra of the as-prepared TiO_2 product.

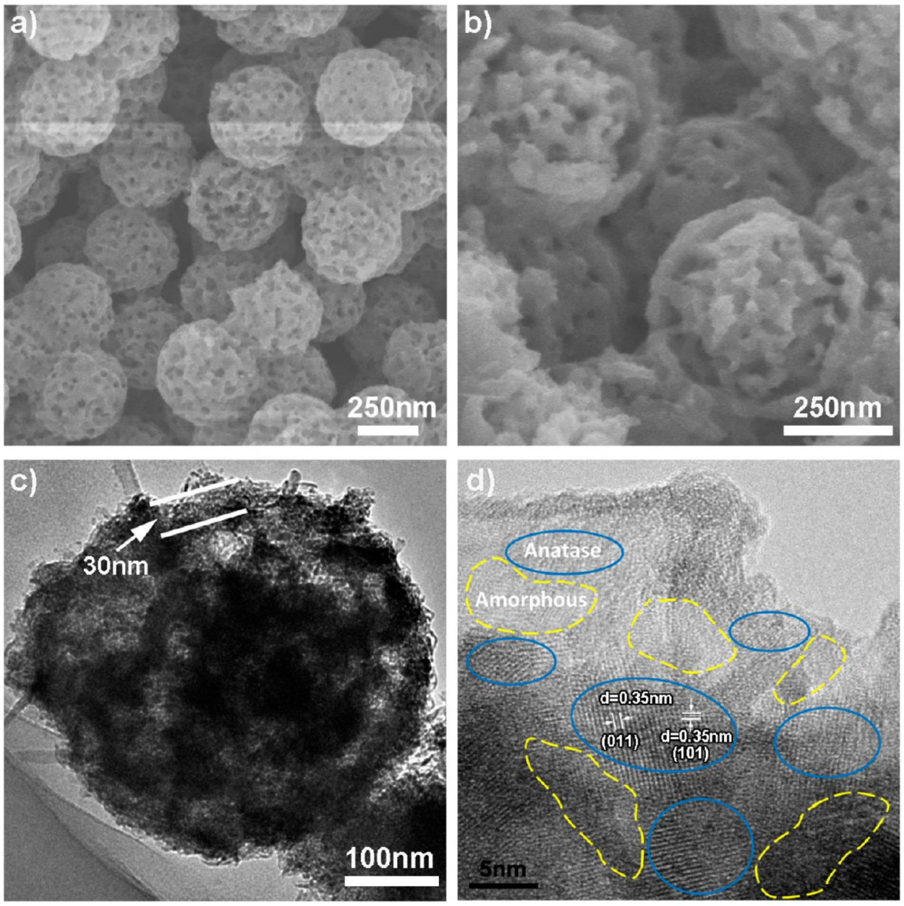

Figure 4. (a, b) SEM images and (c) TEM image of the porous core/shell TiO_2. (d) HRTEM micrograph of the TiO_2 illustrates the anatase nanocrystals are surrounded by some amorphous TiO_2 domains, leading to the formation of abundant nanoscale coherent heterojunctions.

DOI: 10.1021/acsami.6b16498
ACS Appl. Mater. Interfaces 2017, 9, 10652−10663

charge separation and Li^+ intercalation due to the self-building electric field at the phase interfaces.[31,41]

The nitrogen adsorption/desorption isotherms in Figure 5 show a typical type IV curve with H1-type hysteresis, representing typical mesoporous structure.[42] The Brunner–Emmett–Teller (BET) specific surface area of the sample yields to be ~81 m^2 g^{-1}. The Barrett–Joyner–Halenda (BJH) pore size distribution curve (inset of Figure 5) derived from the desorption branch verifies the existence of both macropores and mesopores with size distribution centering at ~35 and 3 nm, respectively, which is in good accordance with the SEM and TEM results.

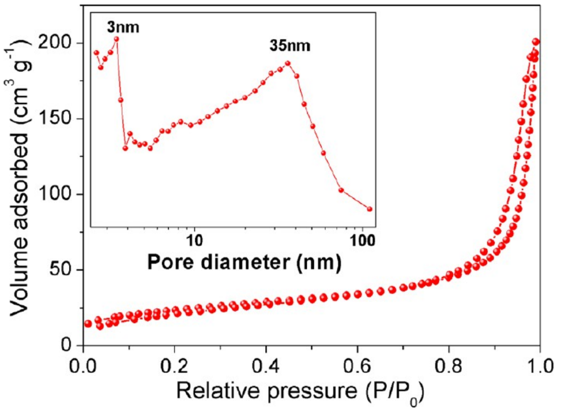

Figure 5. Nitrogen adsorption/desorption isotherms and pore size distribution plot (inset) of the porous core/shell TiO_2.

X-ray photoelectron spectroscopy (XPS) analyses were further conducted to study the elemental composition and chemical states of the elements in the TiO_2 material. Figure 6a shows the XPS spectra at the Ti 2p binding energy (BE) region. The bands centered at 458 and 463.7 eV are ascribed to the $2p_{3/2}$ and $2p_{1/2}$ spin–orbital splitting photoelectrons of Ti^{4+} in TiO_2 lattice. In addition, two other weak peaks centered at 459.5 and 465.2 eV can be attributed to the formation of Ti–C bond[28,29,43,44] due to the *in situ* decomposition of minor oleylamine residue at low annealing temperature. The formation of Ti–C bond and existence of minor carbon species have been further confirmed by C 1s XPS analysis and thermogravimetric analysis/differential scanning calorimetry (TGA/DSC), respectively, as discussed later. The O 1s XPS spectrum (Figure 6b) can be deconvoluted into three bands. The band centered at 530 eV corresponds to the O–Ti bonds while the bands centered at 531.5 and 532.7 eV can be assigned to the C–O–Ti bonds and O–H bonds of surface adsorbed H_2O. Figure 6c depicts the C 1s XPS spectra. The deconvolution of C 1s spectra reveals five different bands. The strongest band centered at 284.9 eV corresponds to the C–C/C═C bonds of graphitic carbon. The band centered at 284.3 eV can be assigned to the bonds of C connected to Ti,[43] signifying the formation of Ti–C bond between the TiO_2 and minor carbon species as discussed above. The presence of Ti–C bonds will favor the electron transfer from carbon to TiO_2 and thus enhance the electronic conduction in the TiO_2

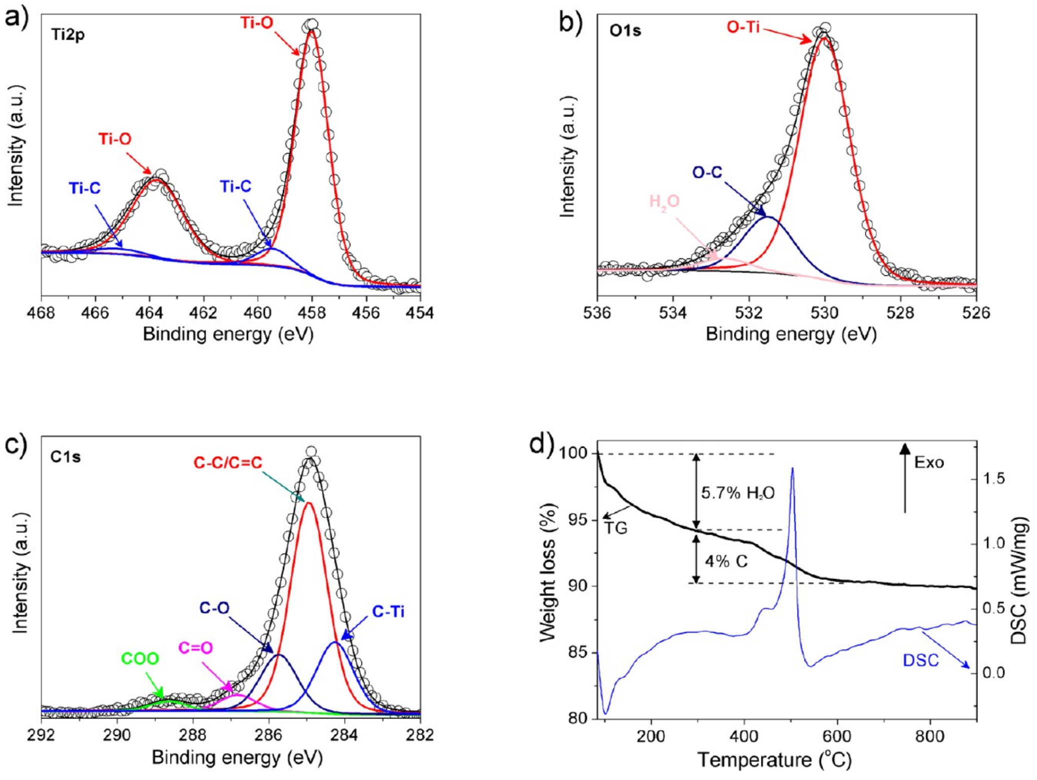

Figure 6. X-ray photoelectron spectra (XPS) of (a) Ti 2p spectrum, (b) O 1s spectrum, and (c) C 1s spectrum in the TiO_2 product, demonstrating the existence of residual carbon species in form of Ti–C bonds with adjacent TiO_2 in the final product. (d) TGA/DSC curves of the TiO_2 material, further confirming the presence of ~5.7 wt % H_2O and ~4 wt % carbon species. The presence of trace carbon species is possibly due to the incomplete thermal decomposition (carbonization) process of oleylamine molecules adsorbed on the inner porous TiO_2 particles' surfaces. The existence of carbon is believed to be beneficial for the electron transport in the TiO_2, leading to improved rate property of the TiO_2 electrode.

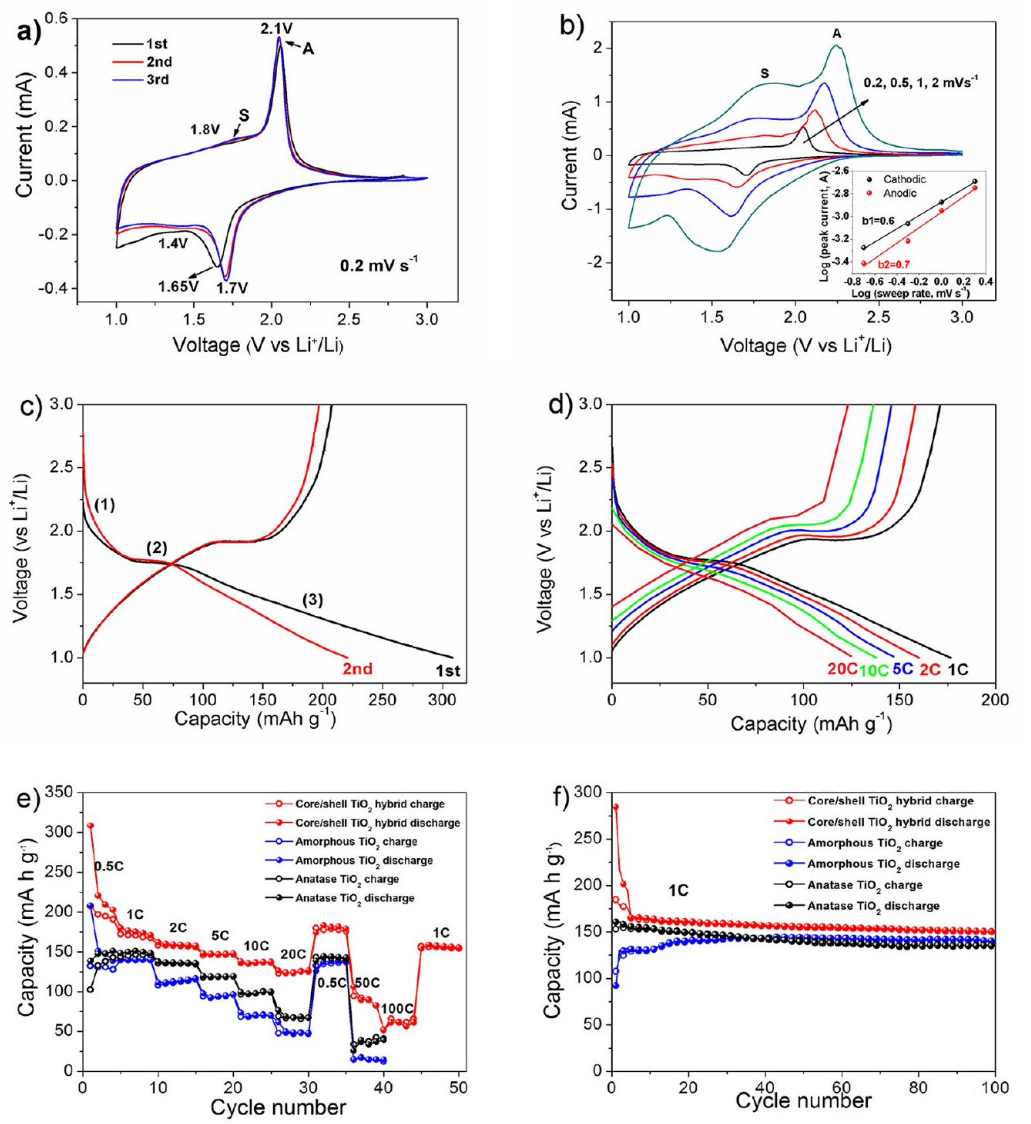

Figure 7. (a) The first three cycles of cyclic voltammetry (CV) curves of the TiO_2 electrode at 0.2 mV s^{-1}; (b) CV curves of the TiO_2 electrode at 0.2, 0.5 1, and 2 mV s^{-1}, respectively; (c) first and second galvanostatic discharge−charge curves of the TiO_2 electrode at 0.5 C (1 C = 170 mA g^{-1}); (d) discharge−charge curves of the TiO_2 electrode at 1, 2, 5, 10, and 20 C, respectively; (e) rate properties and (f) cycling performances of the core/shell TiO_2 hybrid, amorphous TiO_2, and anatase TiO_2 electrodes.

material, which is beneficial for high rate lithium storage. In addition, the C 1s bands centered at 258.7, 286.2, and 288.7 eV correspond to the C−O, C═O, and −COO functional groups on the surface of the carbon species, respectively.[44]

TGA/DSC measurements were used to further identify the carbon content in the TiO_2 sample. As shown in Figure 6d, the initial weight loss of 5.7% before 300 °C can be mainly due to the physically adsorbed water at the porous particle surfaces. The second weight loss of 4% occurring between 300 and 600 °C can be assigned to the combustion of the carbon species contained in the TiO_2 sample, which is accompanied by a large exothermal peak as shown in the DSC curve. It is noted that the elevated decomposition temperature for complete removal of carbon species (600 °C) compared to previous work (480 °C)[29] can be ascribed to the formation of strong Ti−C bonds as shown in XPS (Figure 6a,c).

We then evaluate the lithium storage performance of the porous core/shell TiO_2 electrode in the voltage range of 1−3 V vs Li^+/Li. Figure 7a records the first three cycles of cyclic voltammetry (CV) curves of the TiO_2 electrode at 0.2 mV s^{-1}. In the first cathodic sweep, the Li-insertion potential is noted at 1.65 V vs Li^+/Li. In the subsequent anodic scan, the oxidation peak occurs at 2.1 V vs Li^+/Li (denoted as "A peaks"). In the second cathodic scan, the reduction peak shifts to a higher potential of 1.7 V with slight increased peak current, suggesting an activation process.[20] The potential gap between redox couples becomes smaller and the peak current slightly increases, representing the decreased electrode polarization and improved electrochemical kinetics.[45] As a result, the reversibility of Li^+ insertion/removal increases after the first cycle possibly due to the improved electrolyte permeation in our porous core/shell electrode.[20] The third sweep curve almost overlaps with the second one, implying the highly reversible redox reaction. Besides, another pair of redox peaks is observed at ∼1.4 and 1.8 V (termed as "S peaks"). This peak can be ascribed to pseudocapacitive lithium storage processes that occur in porous nanostructures or amorphous domains.[33] The CV curves of the TiO_2 electrode recorded at varied sweep rates are depicted in

Figure 7b. The well-defined and increased redox peak currents along with increase of sweep rates indicate the very good kinetics of the TiO_2 electrode. In particular, the current values of "S peak" increase much faster with the increase of scan rate than those of the "A peak", suggesting the fast pseudocapacitive process contributes more Li storage in the TiO_2 electrode at high rates. The existence of carbon and Ti−C bond facilitates fast electron transportation, resulting an excellent electrochemical performance at high rates.[29,30] Generally, the dependency of current response with scan rate in CV curves can be used to distinguish the charge storage process according to the equation

$$i = av^b$$

In this equation, current i is fit to a power law with scan rate v, and the exponential term b can be determined from the slope of $\log(i)$ versus $\log(v)$ plot. Usually, a b value of 0.5 indicates a diffusion-controlled Li^+ intercalation process in solid electrode while b value of 1 signifies a surface-mediated pseudocapacitive storage process. In current experiments, the fitted b values for the cathodic and anodic process are 0.6 and 0.7, respectively (inset of Figure 7b), suggesting Li storage is governed by both diffusion in the solid state electrode and pseudocapacitive storage on the surface.

Figure 7c shows the first two galvanostatic discharge/charge voltage profiles of the TiO_2 electrode at 0.5 C (1 C = 170 mA g^{-1}). The discharge curves can be separated into three different regions. The first region shows a monotonous potential drop before reaching a voltage plateau, which relates to a solid−solution insertion mechanism linked to porous nanostructures.[46] The second region with a voltage plateau at ∼1.7 V is associated with Li^+ insertion and occupation of empty interstitial octahedral sites in anatase lattice. During this process a two-phase reaction occurs with an equilibrium between tetragonal $Li_{0.01}TiO_2$ and orthorhombic $Li_{0.55}TiO_2$.[47] In addition, no inflection point is observed before entering the second region, suggesting no extra overpotential is required for driving the initial nucleation of $Li_{0.55}TiO_2$. This result can be ascribed to the enhanced reaction kinetics caused by the presence of carbon content and Ti−C bonds[30] and sintered nanograins in porous core/shell structure, which significantly increase the electrical conduction and shorten the diffusion path lengths of Li^+ ions. The third region with a slope potential drop reflects extra lithium storage at the particle surface[48] as well as the formation of a new Li_1TiO_2 phase.[49] The very long slope region of third stage and the short potential plateau at second region suggest an increased surface Li^+ storage in the porous core/shell TiO_2 due to their high specific surface area, small crystallite size, and the coexistence of amorphous phase. The TiO_2 electrode delivers a high initial discharge capacity of 307 mA h g^{-1} followed by a charge capacity of 208 mA h g^{-1}, with an initial Coulombic efficiency (CE) of 68%. The initially irreversible capacity loss is mainly due to the decomposition of trace moisture adsorbed on the electrode surface and insertion of Li^+ ions into some sites that are not extractable.[37] The discharge and charge capacities are 220.7 and 196.6 mA h g^{-1} in the second cycle, together with a much higher CE of 89%, implying its superior Li storage property. The discharge/charge curve profiles at varied current rates are shown in Figure 7d. It is evident that the as-obtained TiO_2 material exhibits high and reversible Li^+ storage capacity even at very high current rates. In addition, the potential plateaus between discharge and charge increase very slowly, further demonstrating the superior Li^+ insertion/extraction kinetics in the TiO_2 electrode. From the rate capability curve (Figure 7e), the core/shell TiO_2 hybrid electrode delivers reversible capacities of 176.7, 162, 157.7, 135.7, and 126.4 mA h g^{-1} at rates of 1, 2, 5, 10, and 20 C, respectively. Even at an ultrahigh rate of 100 C, the TiO_2 electrode can still deliver 62 mA h g^{-1} (a retention of ∼36.3% relative to the value at 1 C). When the current rate is suddenly reduced to 1 C again, a reversible capacity of 160 mA h g^{-1} can be recovered, indicating the superior cycling stability of the electrode. Moreover, the core/shell TiO_2 electrode also exhibits excellent cycling performance with a reversible capacity of 151 mA h g^{-1} after 100 cycles. As discussed previously, the excellent lithium storage performance of the core/shell TiO_2 electrode is related to the presence of amorphous TiO_2 in the sample, which favors the formation of nanoscale coherent heterointerfaces, enabling fast Li-ion diffusion and electron transport driven by a self-building electric field. To prove these, we further measured the electrochemical properties of amorphous TiO_2 and pure anatase TiO_2 for comparison. The related structures and morphologies of the two control TiO_2 samples have been characterized by XRD, SEM, Raman, and TEM, respectively as shown in Figures S3, S4, S5, and S6. Clearly, the core/shell TiO_2 with hybridized amorphous/anatase phases exhibit better rate capability and cycling property than the amorphous and anatase TiO_2 (Figure 7e,f).

To further reveal the favorable reaction kinetics of the amorphous/anatase TiO_2 electrode, electrochemical impedance spectroscopy (EIS) analyses of the three samples are further provided in Figure 8. The Nyquist plots are composed of a semicircle in the high-frequency region which is related to the charge transfer resistance (R_{ct})[50] and one sloping line in the low-frequency region corresponding to the Li^+ diffusion in the electrode. The plots reveal that the amorphous/anatase TiO_2 electrode has a much smaller R_{ct} value than the amorphous and anatase TiO_2 electrodes, suggesting its better kinetics characteristics. The superior kinetics property of the TiO_2 electrode benefits from the improved electrical conduction and facile Li^+ uptake due to the porous core/shell structure and phase hybridization with nanoscale coherent heterointerfaces as well as the presence of minor carbon species and the formation of Ti−C bonds.

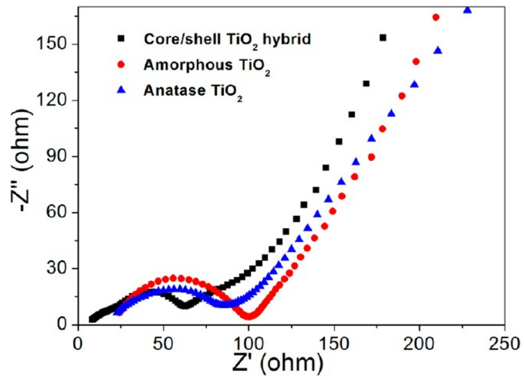

Figure 8. Electrochemical impedance spectra (EIS) of the core/shell TiO_2 hybrid, amorphous TiO_2, and anatase TiO_2 electrodes after activation at 0.5 C for five cycles.

Moreover, long-term cycling performance at high rate is crucial for the practical high-power implementation of lithium-ion batteries. To identify the favorable cyclic stability of the

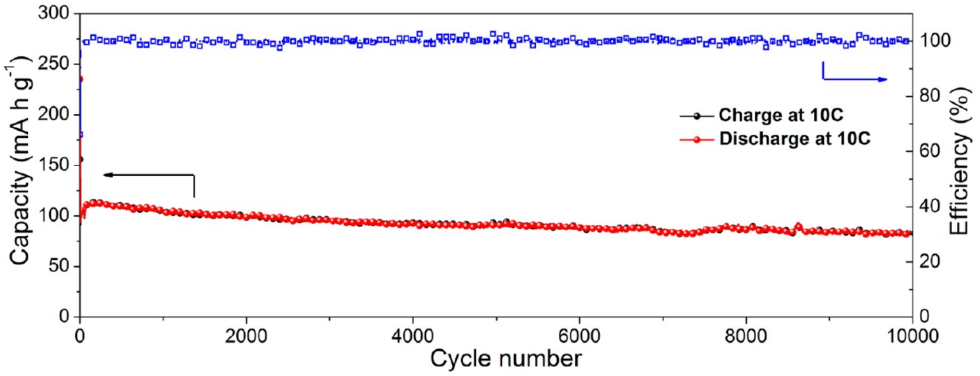

Figure 9. Long-term cycling property of the core/shell TiO_2 hybrid electrode at 10 C for up to 10 000 cycles.

TiO_2 electrode, the Li-half cell is tested up to 10 000 cycles at 10 C. As shown in Figure 9, the TiO_2 electrode delivers an original capacity of 99 mA h g^{-1} and retains a capacity of 83 mA h g^{-1} after 10 000 cycles, demonstrating a high capacity retention of 84% and a very low capacity loss rate of ∼0.002% per cycle. This outstanding cycling stability and rate capability of the TiO_2 electrode are also superior or comparable to a variety of core/shell structured TiO_2 materials[25,26,51−57] reported previously, as summarized in Table 1.

Table 1. Electrochemical Performance Comparison of Our Work with Some Representative TiO_2 Nanostructures from the Relevant Literature

TiO_2 samples	1 C	2 C	5 C	10 C
porous core/shell TiO_2 spheres (this work)	177	162	158	136
multishelled TiO_2 spheres[55]	N/A	237	159	145
TiO_{2-x} hollow microspheres[51]	192	N/A	121	92
anatase@TiO_2(B) core−shell spheres[53]	155	N/A	154	131
yolk−shell TiO_2 porous microspheres[26]	237	213	159	117
yolk−shell TiO_2 hierarchical microspheres[54]	198	N/A	157	127
TiO_2@graphitic-like core−shell nanostructure[56]	75	N/A	∼50	N/A
porous TiO_2/C nanocomposite shells[57]	204	189	168	139
TiO_2−C core−shell nanowires[25]	N/A	145	N/A	56
TiO_2/CNT core−shell nanofibers[52]	170	150	∼100	75

To disclose the effects of repeated electrochemical (de)-lithiation on the morphology and microstructure of the TiO_2 electrode, *ex situ* SEM and TEM characterizations of the TiO_2 electrode after cycling at different current rates were conducted as shown in Figure 10. Figure 10a−c shows the SEM and TEM images of the electrode after cycling at 1 C for 50 cycles. Clearly, the porous morphology and core/shell structure of the TiO_2 material have been well preserved. This observation is strikingly different from the previous findings that obvious structure decay (e.g., evolution of cracks) observed in ordered mesoporous TiO_2 spherical frameworks after discharge/charge for 50 cycles.[58] This result clearly validates the better structural robustness of our porous core/shell material, which is beneficial for superior electrochemical Li^+ storage with long-term cycling stability as discussed above. In addition, as can be seen in Figure 10d, even after 10 000 cycles at 10 C, the porous core/shell structure is well-preserved, indicating the good structural integrity of the TiO_2 electrode. From the HRTEM image in Figure 10e, the interplanar distances of 0.21 and 0.35 nm can be indexed to the (200) plane of cubic Li_1TiO_2 and (101) plane of anatase, respectively. The emergence of cubic $LiTiO_2$ in the tetragonal anatase TiO_2 phase can be further confirmed by the SAED pattern (Figure 10f). The newly emerged cubic $LiTiO_2$ phase (JCPDS No. 74-2257)[59] mainly exists in the form of ∼10 nm nanodots attaching on the electrode surface. The direct observation of nano-$LiTiO_2$ after long-term discharge/recharge process strongly supports the deep lithiation capability of the porous core/shell TiO_2 electrode with coexisted coherent anatase/amorphous heterointerfaces and minor graphitic carbon.

The outstanding electrochemical performance of the TiO_2 material can be ascribed to the unique structural characteristics, as schematically shown in Scheme 2. (i) The porous core/shell structure can serve as an electrolyte reservoir, improve electrode/electrolyte contact, reduce the transport distances of electrons and lithium ions, and buffer the volume variation during (de)lithiation. (ii) The nanoscale coherent anatase/amorphous heterostructures with a self-building electric field can promote the charge transfer and Li^+ insertion at the phase interface. (iii) The presence of amorphous TiO_2 domains can also increase the practical lithium storage capacity. (iv) Finally, the coexistence of minor graphitic carbon species with the formation of Ti−C bonds can increase the electronic conduction among the TiO_2 interparticles and buffer the tiny volume change of TiO_2 during Li^+ insertion/extraction.

3. CONCLUSIONS

Unique hierarchically structured porous TiO_2 material with core/shell configuration and anatase/amorphous phase hybridization was successfully synthesized via a solvothermal route coupled with post-treatment. The Kirkendall effect was proposed to explain the morphology evolution from sodium titanates to hydrogen titanates. Owing to the integrated features of porous and core/shell structures, hybridized anatase/amorphous phase with coherent interface, and the presence of minor carbon species and the formed Ti−C bonds, the resulting TiO_2 material displays superior lithium storage performance. The current strategy may be extended to the design and synthesis of other electrode materials for broad use in (post) lithium batteries and supercapacitors. In addition, the hierarchically porous core/shell structured TiO_2 material may find other applications in sodium ion batteries, photocatalysis, and photovoltaics, etc.

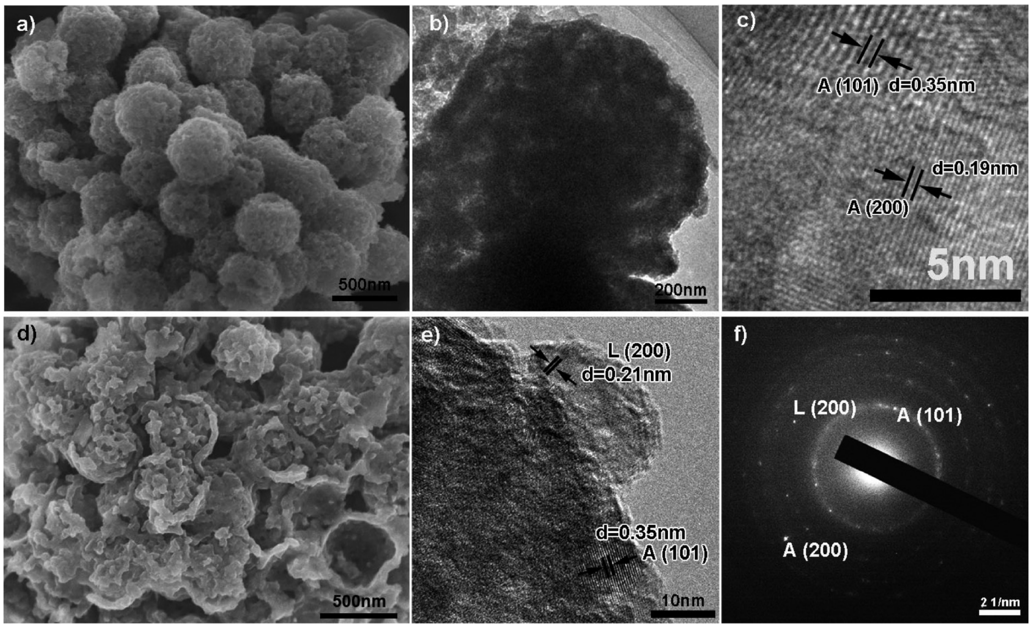

Figure 10. *Ex situ* (a) SEM, (b) TEM, and (c) HRTEM images of the core−shell TiO_2 spheres electrode after cycling at 1 C for 50 cycles and (d) SEM, (e) HRTEM images, and (f) selected-area electron diffraction (SAED) pattern of the core−shell TiO_2 spheres electrode after galvanostatic cycling at 10 C for 10 000 cycles.

Scheme 2. Illustration of Lithium Insertion Mechanism in the Core−Shell TiO_2 Material with Fast Electron Transportation, Large Electrode−Electrolyte Contact Area, and Shortened Li Ion Transport Pathways

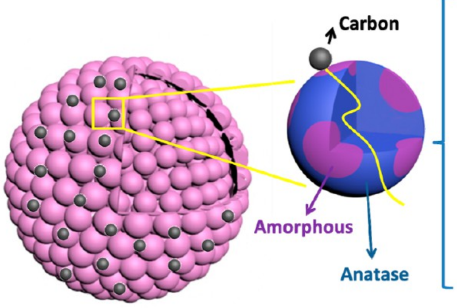

(1)Porous core/shell structure can serve as an electrolyte reservoir and shorten the transport paths of Li ions and electrons, as well as buffer the volume change during charge/discharge;

(2)The charge transport and Li ion insertion capability can be improved at the nanoscale anatase/amorphous heterojunctions driven by a self-building electric field;

(3)The presence of minor carbon species and the formation of Ti-C bonds boost the electronic conductivity of the TiO_2 material.

4. EXPERIMENTAL SECTION

4.1. Synthesis. All the reagents were analytical pure grade and used as received.

First, amorphous spherical TiO_2 particles were prepared by pouring 4.5 mL of tetrabutyl titanate into 200 mL of ethanol solution containing 0.8 mL of deionized (DI) water and 1.8 mL of oleylamine under vigorous stirring. After reaction for 2 h, the resulting white precipitates were washed with absolute ethanol for three times, then collected by centrifugation, and finally dried at 60 °C in air overnight.

Next, sodium titanates (NaTiO) were prepared by a solvothermal reaction. First, 0.25 g of precursor was dispersed in 40 mL of alkaline solution containing 24 g of sodium hydroxide. Then 20 mL of ethanol was added in the solution to form milky suspension under mild stirring. After that, the suspension was transferred to a 100 mL Teflon-lined autoclave and then heated in an electric oven at 150 °C for 48 h. After the autoclave was cooled down, the products were collected by centrifugation, washed with ethanol and deionized water for several times, and finally dried at 60 °C in air. Hydrogenated titanates (HTiO) were prepared by soaking the NaTiO in 0.12 M HCl solution for 12 h, then collected by centrifugation and rinsing with deionized water several times, and finally dried at 60 °C in air.

The porous core/shell TiO_2 material was obtained by annealing the HTiO product at 300 °C for 2 h in air. For comparison, amorphous TiO_2 material was also prepared at the same condition except further increasing the content of sodium hydroxide to 28.8 g. The crystalline anatase TiO_2 material was obtained at the same condition except annealing the HTO product at 450 °C for 6 h in air.

4.2. Characterizations. X-ray diffraction (XRD) patterns were obtained on a Bruker diffractometer at 40 mA/kV with Cu Kα radiation (λ = 0.154 05 nm). The morphologies of the samples were observed by a field-emission scanning electron microscope (FESEM, Hitachi S-4800) equipped with an energy-dispersive X-ray (EDX) spectroscopy. Transmission electron microscopy (TEM) images were acquired on a JEM-2100F electron microscope operated at 200 kV. The surface electronic states of the elements were analyzed by an X-ray photoelectron spectroscope (XPS, Thermo fisher, Alpha). The binding energy (BE) for the sample was calibrated using the C 1s peak from a carbon tape at 284.8 eV. Thermogravimetric analysis (TGA) and differential scanning calorimetry (DSC) curves of the material were performed using a Labsys EvoS60/58458 thermal analysis instrument at a temperature ramping rate of 5 °C min^{-1} in air. Raman spectroscopy measurement was recorded by a Nexus FTIR spectrometer using a laser with wavelength of 1064 nm and resolution of 4 cm^{-1}. Nitrogen adsorption/desorption isotherms were measured at 77 K using a Tri Star II 3020 surface area and porosity analyzer. Prior to adsorption experiments, the samples were degassed at 100 °C for 48 h in a vacuum line. The specific surface area and pore size distribution were calculated by Brunauer−Emmett−Teller (BET) and Barrett−Joyner−Halenda (BJH) methods, respectively.

4.3. Electrochemical Measurements. Electrochemical tests were performed using 2025-type coin cells. The working electrodes were prepared by mixing the active materials, acetylene black, and poly(vinylidene fluoride) (PVDF) with a weight ratio of 7:2:1 in *N*-methyl-2-pyrrolidone (NMP) to form a slurry. The slurry was uniformly spread on a copper foil. Lithium foil was used as the counter electrode and reference electrode. A 1 M solution of $LiPF_6$ dissolved in ethylene carbonate and dimethyl carbonate (1:1 in volume ratio) was used as the electrolyte. The lithium half-cells were assembled in an argon-filled glovebox with both water and oxygen contents below 0.5 ppm. Cyclic voltammetry (CV) data were recorded using an CHI 604e electrochemical workstation. Galvanostatic discharge−charge curves were collected on a LAND CT2001A battery test system within a voltage range of 3.0−1.0 V (vs Li^+/Li) at various C rates (1 C is defined as 170 mA g^{-1}). Electrochemical impedance spectra (EIS) were carried out on an electrochemical workstation (Autolab PGSTAT 302N) in the frequency range of 100 kHz−10 mHz with an amplitude of 5 mV. All the electrochemical measurements were carried out at room temperature.

■ ASSOCIATED CONTENT

Supporting Information

The Supporting Information is available free of charge on the ACS Publications website at DOI: 10.1021/acsami.6b16498.

> SEM images of the sodium titanate (NaTiO) collected after different reaction durations and HRTEM image of the TiO_2 product; XRD patterns, SEM images, and Raman spectrum of amorphous and anatase TiO_2 (PDF)

■ AUTHOR INFORMATION

Corresponding Authors

*Fax +86 27 87879468; Tel +86 27 87855322; e-mail hongen.wang@gmail.com (H.-E.W.).
*Fax +1 206 543 3100; Tel +1 206 616 9084; e-mail gzcao@u.washington.edu (G.C.).
*Fax +32 81 725414; Tel +32 81 724531; e-mail bao-lian.su@unamur.be (B.-L.S.).

ORCID

Hong-En Wang: 0000-0002-6859-5683
Guozhong Cao: 0000-0003-1498-4517

Notes

The authors declare no competing financial interest.

■ ACKNOWLEDGMENTS

B.-L.S. acknowledges the Chinese Central Government for an “Expert of the State” position in the Program of the “Thousand Talents” and a Clare Hall Life Membership at the Clare Hall and the financial support of the Department of Chemistry, University of Cambridge. H.-E.W. and Y.L. acknowledge Hubei Provincial Department of Education for the “Chutian Scholar” program. This work is supported by the National Key Research and Development Program of China (2016YFA0202602), Program for Changjiang Scholars and Innovative Research Team in University (IRT_15R52), the National Science Foundation of China (51302204), and International Science & Technology Cooperation Program of China (2015DFE52870). H.-E.W., X.Z., and F.H. also thank China Scholarship Council (CSC) for financial support for their study at University of Washington, Seattle, WA.

■ REFERENCES

(1) Liu, C.; Neale, Z. G.; Cao, G. Understanding Electrochemical Potentials of Cathode Materials in Rechargeable Batteries. *Mater. Today* **2015**, *19*, 109−123.

(2) Yoshio, M.; Wang, H.; Fukuda, K. Spherical Carbon-Coated Natural Graphite as a Lithium-Ion Battery-Anode Material. *Angew. Chem.* **2003**, *115*, 4335−4338.

(3) Wu, P.; Wang, H.; Tang, Y.; Zhou, Y.; Lu, T. Three-Dimensional Interconnected Network of Graphene-Wrapped Porous Silicon Spheres: In Situ Magnesiothermic-Reduction Synthesis and Enhanced Lithium-Storage Capabilities. *ACS Appl. Mater. Interfaces* **2014**, *6*, 3546−3552.

(4) Zhang, W.; Zhu, X.; Chen, X.; Zhou, Y.; Tang, Y.; Ding, L.; Wu, P. Cyano-Bridged Coordination Polymer Hydrogel-Derived Sn-Fe Binary Oxide Nanohybrids with Structural Diversity: From 3D, 2D, to 2D/1D and Enhanced Lithium-Storage Performance. *Nanoscale* **2016**, *8*, 9828−9836.

(5) Poizot, P.; Laruelle, S.; Grugeon, S.; Dupont, L.; Tarascon, J. M. Nano-Sized Transition-Metal Oxides as Negative-Electrode Materials for Lithium-Ion Batteries. *Nature* **2000**, *407*, 496−499.

(6) Zhao, X.; Sui, J.; Li, F.; Fang, H. T.; Wang, H.; Li, J.; Cai, W.; Cao, G. Lamellar $MoSe_2$ Nanosheets Embedded with MoO_2 Nanoparticles: Novel Hybrid Nanostructures Promoted Excellent Performances for Lithium Ion Batteries. *Nanoscale* **2016**, *8*, 17902−17910.

(7) Zhu, Q.; Wu, P.; Zhang, J.; Zhang, W.; Zhou, Y.; Tang, Y.; Lu, T. Cyanogel-Derived Formation of 3D Nanoporous SnO_2-M_xO_y (M = Ni, Fe, Co) Hybrid Networks for High-Performance Lithium Storage. *ChemSusChem* **2015**, *8*, 131−137.

(8) Aravindan, V.; Lee, Y. S.; Yazami, R.; Madhavi, S. TiO_2 Polymorphs in ‘Rocking-Chair’ Li-Ion Batteries. *Mater. Today* **2015**, *18*, 345−351.

(9) Wagemaker, M.; Mulder, F. M. Properties and Promises of Nanosized Insertion Materials for Li-Ion Batteries. *Acc. Chem. Res.* **2013**, *46*, 1206−1215.

(10) Cao, F. F.; Guo, Y. G.; Wan, L. J. Better Lithium-Ion Batteries with Nanocable-Like Electrode Materials. *Energy Environ. Sci.* **2011**, *4*, 1634−1642.

(11) Cao, F. F.; Xin, S.; Guo, Y. G.; Wan, L. J. Wet Chemical Synthesis of Cu/TiO_2 Nanocomposites with Integrated Nano-Current-Collectors as High-Rate Anode Materials in Lithium-Ion Batteries. *Phys. Chem. Chem. Phys.* **2011**, *13*, 2014−2020.

(12) Guo, Y. G.; Hu, J. S.; Wan, L. J. Nanostructured Materials for Electrochemical Energy Conversion and Storage Devices. *Adv. Mater.* **2008**, *20*, 2878−2887.

(13) Wang, D.; Choi, D.; Yang, Z.; Viswanathan, V. V.; Nie, Z.; Wang, C.; Song, Y.; Zhang, J. G.; Liu, J. Synthesis and Li-Ion Insertion Properties of Highly Crystalline Mesoporous Rutile TiO_2. *Chem. Mater.* **2008**, *20*, 3435−3442.

(14) Wang, J.; Polleux, J.; Lim, J.; Dunn, B. Pseudocapacitive Contributions to Electrochemical Energy Storage in TiO_2 (Anatase) Nanoparticles. *J. Phys. Chem. C* **2007**, *111*, 14925−14931.

(15) Lan, Y.; Gao, X. P.; Zhu, H. Y.; Zheng, Z. F.; Yan, T. Y.; Wu, F.; Ringer, S. P.; Song, D. Y. Titanate Nanotubes and Nanorods Prepared from Rutile Powder. *Adv. Funct. Mater.* **2005**, *15*, 1310−1318.

(16) Armstrong, A. R.; Armstrong, G.; Canales, J.; García, R.; Bruce, P. G. Lithium-Ion Intercalation into TiO_2-B Nanowires. *Adv. Mater.* **2005**, *17*, 862−865.

(17) Ortiz, G. F.; Hanzu, I.; Djenizian, T.; Lavela, P.; Tirado, J. L.; Knauth, P. Alternative Li-Ion Battery Electrode Based on Self-Organized Titania Nanotubes. *Chem. Mater.* **2009**, *21*, 63−67.

(18) Lu, Z.; Yip, C. T.; Wang, L.; Huang, H.; Zhou, L. Hydrogenated TiO_2 Nanotube Arrays as High-Rate Anodes for Lithium-Ion Microbatteries. *ChemPlusChem.* **2012**, *77*, 991−1000.

(19) Cao, F. F.; Guo, Y. G.; Zheng, S. F.; Wu, X. L.; Jiang, L. Y.; Bi, R. R.; Wan, L. J.; Maier, J. Symbiotic Coaxial Nanocables: Facile Synthesis and an Efficient and Elegant Morphological Solution to the Lithium Storage Problem. *Chem. Mater.* **2010**, *22*, 1908−1914.

(20) Chen, J. S.; Lou, X. W. Anatase TiO$_2$ Nanosheet: An Ideal Host Structure for Fast and Efficient Lithium Insertion/Extraction. *Electrochem. Commun.* **2009**, *11*, 2332−2335.

(21) Han, C.; Yang, D.; Yang, Y.; Jiang, B.; He, Y.; Wang, M.; Song, A. Y.; He, Y.; Li, B.; Lin, Z. Hollow Titanium Dioxide Spheres as Anode Material for Lithium Ion Battery with Largely Improved Rate Stability and Cycle Performance by Suppressing the Formation of Solid Electrolyte Interface Layer. *J. Mater. Chem. A* **2015**, *3*, 13340−13349.

(22) Hu, H.; Yu, L.; Gao, X.; Lin, Z.; Lou, X. W. Hierarchical Tubular Structures Constructed from Ultrathin TiO$_2$ (B) Nanosheets for Highly Reversible Lithium Storage. *Energy Environ. Sci.* **2015**, *8*, 1480−1483.

(23) Cai, Y.; Wang, H. E.; Jin, J.; Huang, S. Z.; Yu, Y.; Li, Y.; Feng, S. P.; Su, B. L. Hierarchically Structured Porous TiO$_2$ Spheres Constructed by Interconnected Nanorods as High Performance Anodes for Lithium Ion Batteries. *Chem. Eng. J.* **2015**, *281*, 844−851.

(24) Cai, Y.; Wang, H. E.; Huang, S. Z.; Yuen, M. F.; Cai, H. H.; Wang, C.; Yu, Y.; Li, Y.; Zhang, W. J.; Su, B. L. Porous TiO$_2$ Urchins for High Performance Li-Ion Battery Electrode: Facile Synthesis, Characterization and Structural Evolution. *Electrochim. Acta* **2016**, *210*, 206−214.

(25) Liao, J. Y.; Higgins, D.; Lui, G.; Chabot, V.; Xiao, X.; Chen, Z. Multifunctional TiO$_2$-C/MnO$_2$ Core-Double-Shell Nanowire Arrays as High-Performance 3D Electrodes for Lithium Ion Batteries. *Nano Lett.* **2013**, *13*, 5467−5473.

(26) Jin, J.; Huang, S. Z.; Li, Y.; Tian, H.; Wang, H. E.; Yu, Y.; Chen, L. H.; Hasan, T.; Su, B. L. Hierarchical Nanosheet-Constructed Yolk-Shell TiO$_2$ Porous Microspheres for Lithium Batteries with High Capacity, Superior Rate and Long Cycle Capability. *Nanoscale* **2015**, *7*, 12979−12989.

(27) Cao, F. F.; Wu, X. L.; Xin, S.; Guo, Y. G.; Wan, L. J. Facile Synthesis of Mesoporous TiO$_2$-C Nanosphere as an Improved Anode Material for Superior High Rate 1.5 V Rechargeable Li Ion Batteries Containing Lifepo$_4$-C Cathode. *J. Phys. Chem. C* **2010**, *114*, 10308−10313.

(28) Huang, Y.; Ho, W.; Lee, S. C.; Zhang, L. Z.; Li, G. S.; Yu, J. C. Effect of Carbon Doping on the Mesoporous Structure of Nanocrystalline Titanium Dioxide and Its Solar-Light-Driven Photocatalytic Degradation of NO$_x$. *Langmuir* **2008**, *24*, 3510−3516.

(29) Huang, H. B.; Yang, Y.; Chen, L. H.; Wang, Y.; Huang, S. Z.; Tao, J. W.; Ma, X. T.; Hasan, T.; Li, Y.; Xu, Y.; Su, B. L. Hierarchical TiO$_2$/C Nanocomposite Monoliths with a Robust Scaffolding Architecture, Mesopore-Macropore Network and TiO$_2$-C Heterostructure for High-Performance Lithium Ion Batteries. *Nanoscale* **2016**, *8*, 10928−10937.

(30) Etacheri, V.; Yourey, J. E.; Bartlett, B. M. Chemically Bonded TiO$_2$-Bronze Nanosheet/Reduced Graphene Oxide Hybrid for High-Power Lithium Ion Batteries. *ACS Nano* **2014**, *8*, 1491−1499.

(31) Zhou, T.; Zheng, Y.; Gao, H.; Min, S.; Li, S.; Liu, H. K.; Guo, Z. Surface Engineering and Design Strategy for Surface-Amorphized TiO$_2$@Graphene Hybrids for High Power Li-Ion Battery Electrodes. *Adv. Sci.* **2015**, *2*, 1500027.

(32) Song, W.; Chen, J.; Ji, X.; Zhang, X.; Xie, F.; Riley, D. J. Dandelion-Shaped TiO$_2$/Multi-Layer Graphene Composed of TiO$_2$ (B) Fibrils and Anatase TiO$_2$ Pappi Utilizing Triphase Boundaries for Lithium Storage. *J. Mater. Chem. A* **2016**, *4*, 8762−8768.

(33) Wu, Q.; Xu, J.; Yang, X.; Lu, F.; He, S.; Yang, J.; Fan, H. J.; Wu, M. Ultrathin Anatase TiO$_2$ Nanosheets Embedded with TiO$_2$-B Nanodomains for Lithium-Ion Storage: Capacity Enhancement by Phase Boundaries. *Adv. Energy Mater.* **2015**, *5*, 1401756.

(34) Yan, Z.; Liu, L.; Tan, J.; Zhou, Q.; Huang, Z.; Xia, D.; Shu, H.; Yang, X.; Wang, X. One-Pot Synthesis of Bicrystalline Titanium Dioxide Spheres with a Core/Shell Structure as Anode Materials for Lithium and Sodium Ion Batteries. *J. Power Sources* **2014**, *269*, 37−45.

(35) Sutradhar, N.; Sinhamahapatra, A.; Pahari, S. K.; Bajaj, H. C.; Panda, A. B. Room Temperature Synthesis of Protonated Layered Titanate Sheets Using Peroxo Titanium Carbonate Complex Solution. *Chem. Commun.* **2011**, *47*, 7731−7733.

(36) Qiu, P.; Li, W.; Thokchom, B.; Park, B.; Cui, M.; Zhao, D.; Khim, J. Uniform Core-Shell Structured Magnetic Mesoporous TiO$_2$ Nanospheres as a Highly Efficient and Stable Sonocatalyst for the Degradation of Bisphenol-A. *J. Mater. Chem. A* **2015**, *3*, 6492−6500.

(37) Wang, H. E.; Cheng, H.; Liu, C. P.; Chen, X.; Jiang, Q. L.; Lu, Z. G.; Li, Y. Y.; Chung, C. Y.; Zhang, W. J.; Zapien, J. A.; Martinu, L.; Bello, I. Facile Synthesis and Electrochemical Characterization of Porous and Dense TiO$_2$ Nanospheres for Lithium-Ion Battery Applications. *J. Power Sources* **2011**, *196*, 6394−6399.

(38) Wang, H. E.; Lu, Z. G.; Xi, L. J.; Ma, R. G.; Wang, C. D.; Zapien, J. A.; Bello, I. Facile and Rapid Synthesis of Highly Porous Wirelike TiO$_2$ as Anodes for Lithium-Ion Batteries. *ACS Appl. Mater. Interfaces* **2012**, *4*, 1608−1613.

(39) Huang, S. Z.; Zhang, L.; Lu, X.; Liu, L.; Liu, L.; Sun, X.; Yin, Y.; Oswald, S.; Zou, Z.; Ding, F. Tunable Pseudocapacitance in 3D TiO$_{2-\delta}$ Nanomembranes Enabling Superior Lithium Storage Performance. *ACS Nano* **2017**, *11*, 821−830.

(40) Fang, H. T.; Liu, M.; Wang, D. W.; Sun, T.; Guan, D. S.; Li, F.; Zhou, J.; Sham, T. K.; Cheng, H. M. Comparison of the Rate Capability of Nanostructured Amorphous and Anatase TiO$_2$ for Lithium Insertion Using Anodic TiO$_2$ Nanotube Arrays. *Nanotechnology* **2009**, *20*, 225701.

(41) Zheng, Y.; Zhou, T.; Zhang, C.; Mao, J.; Liu, H.; Guo, Z. Boosted Charge Transfer in SnS/SnO$_2$ Heterostructures: Toward High Rate Capability for Sodium-Ion Batteries. *Angew. Chem., Int. Ed.* **2016**, *55*, 3408−3413.

(42) Liu, H.; Bi, Z.; Sun, X. G.; Unocic, R. R.; Paranthaman, M. P.; Dai, S.; Brown, G. M. Mesoporous TiO$_2$-B Microspheres with Superior Rate Performance for Lithium Ion Batteries. *Adv. Mater.* **2011**, *23*, 3450−3454.

(43) Chen, L. C.; Ho, Y. C.; Guo, W. S.; Huang, C. M.; Pan, T. C. Enhanced Visible Light-Induced Photoelectrocatalytic Degradation of Phenol by Carbon Nanotube-Doped TiO$_2$ Electrodes. *Electrochim. Acta* **2009**, *54*, 3884−3891.

(44) Akhavan, O.; Ghaderi, E. Photocatalytic Reduction of Graphene Oxide Nanosheets on TiO$_2$ Thin Film for Photoinactivation of Bacteria in Solar Light Irradiation. *J. Phys. Chem. C* **2009**, *113*, 20214−20220.

(45) Lian, P.; Zhu, X.; Liang, S.; Li, Z.; Yang, W.; Wang, H. High Reversible Capacity of SnO/Graphene Nanocomposite as an Anode Material for Lithium-Ion Batteries. *Electrochim. Acta* **2011**, *56*, 4532−4539.

(46) Sudant, G.; Baudrin, E.; Larcher, D.; Tarascon, J. M. Electrochemical Lithium Reactivity with Nanotextured Anatase-Type TiO$_2$. *J. Mater. Chem.* **2005**, *15*, 1263−1269.

(47) Wagemaker, M.; Kentgens, A. P. M.; Mulder, F. M. Equilibrium Lithium Transport between Nanocrystalline Phases in Intercalated TiO$_2$ Anatase. *Nature* **2002**, *418*, 397−399.

(48) Shin, J. Y.; Samuelis, D.; Maier, J. Sustained Lithium-Storage Performance of Hierarchical, Nanoporous Anatase TiO$_2$ at High Rates: Emphasis on Interfacial Storage Phenomena. *Adv. Funct. Mater.* **2011**, *21*, 3464−3472.

(49) Wagemaker, M.; Borghols, W. J.; Mulder, F. M. Large Impact of Particle Size on Insertion Reactions. A Case for Anatase Li$_x$TiO$_2$. *J. Am. Chem. Soc.* **2007**, *129*, 4323−4327.

(50) Ma, Y.; Fang, C.; Ding, B.; Ji, G.; Lee, J. Y. Fe-Doped Mn$_x$O$_y$ with Hierarchical Porosity as a High-Performance Lithium-Ion Battery Anode. *Adv. Mater.* **2013**, *25*, 4646−4652.

(51) Wang, C.; Wang, F.; Zhao, Y.; Li, Y.; Yue, Q.; Liu, Y.; Liu, Y.; Elzatahry, A. A.; Al-Enizi, A.; Wu, Y. Hollow TiO$_{2\text{-x}}$ Porous Microspheres Composed of Well-Crystalline Nanocrystals for High-Performance Lithium-Ion Batteries. *Nano Res.* **2016**, *9*, 165−173.

(52) Qing, R.; Liu, L.; Kim, H.; Sigmund, W. M. Electronic Property Dependence of Electrochemical Performance for TiO$_2$/CNT Core-Shell Nanofibers in Lithium Ion Batteries. *Electrochim. Acta* **2015**, *180*, 295−306.

(53) Yan, Z.; Liu, L.; Tan, J.; Zhou, Q.; Huang, Z.; Xia, D.; Shu, H.; Yang, X.; Wang, X. One-Pot Synthesis of Bicrystalline Titanium

Dioxide Spheres with a Core-Shell Structure as Anode Materials for Lithium and Sodium Ion Batteries. *J. Power Sources* **2014**, *269*, 37−45.

(54) Wang, X.; Wang, Y.; Yang, L.; Wang, K.; Lou, X.; Cai, B. Template-Free Synthesis of Homogeneous Yolk-Shell TiO_2 Hierarchical Microspheres for High Performance Lithium Ion Batteries. *J. Power Sources* **2014**, *262*, 72−78.

(55) Ren, H.; Yu, R.; Wang, J.; Jin, Q.; Yang, M.; Mao, D.; Kisailus, D.; Zhao, H.; Wang, D. Multishelled TiO_2 Hollow Microspheres as Anodes with Superior Reversible Capacity for Lithium Ion Batteries. *Nano Lett.* **2014**, *14*, 6679−6684.

(56) Kim, M. C.; Lee, Y. W.; Kim, S. J.; Hwang, B. M.; Park, H. C.; Hwang, E. T.; Cao, G.; Park, K. W. Improved Lithium Ion Behavior Properties of TiO_2@Graphitic-Like Carbon Core@Shell Nanostructure. *Electrochim. Acta* **2014**, *147*, 241−249.

(57) Wang, W.; Sa, Q.; Chen, J.; Wang, Y.; Jung, H.; Yin, Y. Porous TiO_2/C Nanocomposite Shells as a High-Performance Anode Material for Lithium-Ion Batteries. *ACS Appl. Mater. Interfaces* **2013**, *5*, 6478−6483.

(58) Yonemoto, B. T.; Guo, Q.; Hutchings, G. S.; Yoo, W. C.; Snyder, M. A.; Jiao, F. Structural Evolution in Ordered Mesoporous TiO_2 Anatase Electrodes. *Chem. Commun.* **2014**, *50*, 8997−8999.

(59) Gao, Q.; Gu, M.; Nie, A.; Mashayek, F.; Wang, C.; Odegard, G. M.; Shahbazianyassar, R. Direct Evidence of Lithium-Induced Atomic Ordering in Amorphous TiO_2 Nanotubes. *Chem. Mater.* **2014**, *26*, 1660−1669.